CANMILK

GREENHOUSE GAS REDUCTION IN AGRICULTURE
USING PLASMA-BASED SOLUTIONS

DELIVERABLE D2.1

CHEMICAL KINETICS AND COMPUTATIONAL FLUID DYNAMICS MODEL

PROJECT GRANT AGREEMENT NO	DUE DATE OF DELIVERABLE:	ACTUAL SUBMISSION DATE:	START DATE OF PROJECT:	PROJECT DURATION:
101069491	31.01.2024	31.01.2024	01.09.2022	48 MONTHS

Funded by
the European Union

Work Package	2
Associated Task	2.1
Deliverable Lead Partner	Prof. Annemie Bogaerts
Main author(s)	Matthias Albrechts
Internal Reviewer(s)	Ivan Tsonev
Version	2.0

DISSEMINATION LEVEL		
PU	Public	X
PP	Restricted to other programme participants (including the Commission Services)	
RE	Restricted to a group specified by the consortium (including the Commission Services)	
CO	Confidential, only for members of the consortium (including the Commission Services)	

CHANGE CONTROL

DOCUMENT HISTORY

VERSION	DATE	CHANGE HISTORY	AUTHOR	ORGANISATION
1.0	16/1/2024	Original	Matthias Albrechts	University of Antwerp
2.0	10/9/2024	Updated according to comments received during the review of 1st reporting period: - Added description of the plug flow reactor to section 2.1.1 - Improved and modified section 2.1.1.3 to explain the afterglow and the implications of the modelling results on the proposed CANMILK system. - Improved and modified section 2.1.2.2 to further explain afterglow properties. - Added discussion about alternative strategies to both section 2.1.2.2 and to conclusions. - Several small changes such as updating the numbering of Figures and other minor corrections.	Matthias Albrechts	University of Antwerp

This deliverable is part of a project that has received funding from the European Union's Horizon Europe research and innovation programme under grant agreement no 101069491.

EXECUTIVE SUMMARY

We have developed two distinct chemical kinetics models. The first focuses on the O_2 plasma chemistry, examining the O atom density in the plasma and its afterglow. The second model details the mixing of the O_2 afterglow with the barn air mixture, investigating the conversion of low CH_4 fractions through O atom activation. In addition to the chemical kinetics models, we have built a computational fluid dynamics (CFD) model to assess the mixing performance of the experimental reactor setup used at Maastricht University.

DEVIATIONS

No.

TABLE OF CONTENT

LIST OF FIGURES

LIST OF ABBREVATIONS

ACRONYM	DESCRIPTION
CFD	Computational fluid dynamics
D	Deliverable
EC	European Commission
ROS	Reactive oxygen species

WP	Work package
T	Task

1 INTRODUCTION

WP2 of the CANMILK project is responsible for the development of the plasma technology. In the current concept, oxygen plasma is employed to generate O atoms, and subsequently, through the mixing of the O_2 afterglow with the barn air containing low CH_4 concentrations, the O atoms are titrated to the barn air and CH_4 removal is initiated. The CH_4 conversion, diluted in air, is investigated through a combination of modeling at the University of Antwerp and plasma diagnostics experiments performed at the University of Maastricht (UM). Since the D2.1 deliverable involves the development of a chemical kinetics model and a CFD model, the work discussed below is conducted exclusively by the University of Antwerp. Future stages will involve the comparison of modeling calculations with experimental measurements from the University of Maastricht, to gain insight into the experimental results and to guide the reactor development.

1.1 T2.1: CHEMICAL KINETICS MODEL

To describe the post-plasma conversion of methane impurities in the barn air, we developed two distinct chemical kinetics models. In the first model, we study the oxygen plasma kinetics, with the aim of investigating the creation of reactive oxygen species (ROS) and evaluating how long these ROS survive in the plasma afterglow. The composition of the oxygen plasma afterglow, obtained from the first model, serves as input to the second model, in which we characterize the mixing of the hot plasma afterglow with the CH_4 containing atmosphere, and evaluate how efficiently the ROS, i.e. O atoms, convert the low CH_4 fraction.

1.2 T2.2: COMPUTATIONAL FLUID DYNAMICS MODEL

In addition to the above chemical kinetics models, predicting the post-plasma conversion, we also developed a CFD model, in order to evaluate the mixing of the O_2 plasma afterglow with the barn air mixture. As the chemical kinetics modeling results indicate that rapid mixing is crucial for efficient CH_4 conversion and reduced NO_x formation, as will be discussed below (2.1.2), the developed CFD model can be utilized to optimize the reactor geometry for enhanced mixing of the plasma afterglow and barn air.

2 DESCRIPTION OF ACTIVITIES

2.1 T2.1: CHEMICAL KINETICS MODEL

2.1.1 MODEL 1: OXYGEN PLASMA MODEL

Since we are utilizing a thermal plasma for the project, i.e. a microwave torch, we aim to use the O atoms in the plasma afterglow as ROS for the post-plasma conversion of CH_4. To study the O atom creation inside the plasma and to evaluate how far the O atoms travel in the plasma afterglow, we have developed a pseudo-1D plug flow kinetic model in the framework of the plasma module of COMSOL Multiphysics. By means of the gas flow velocity, the time-dependent evolution of the species densities inside the simulated plug-element can be translated to a distance travelled in the reactor. A paper about this model was published in Plasma Sources Science and Technology.

Before taking a deeper look into the model implementations and modeling results, we make a clear link between our plug-flow kinetic model and the experimental reactor set-up. Figure 1 shows the experimental set-up of UM and its relationship to the plug position within our kinetic simulation. The start of the MW cavity, i.e., the discharge, corresponds to the start point of the simulation (x = 0). As the simulation progresses, the gas moves along the plug, i.e. the longitudinal direction of the reactor tube, where the simulation variables describe the state in the plug-element, i.e. the reactor cross-section at the given position x in the plug, as indiated in figure 1, assuming radial uniformity. The end of the discharge corresponds to x = 4 cm in the kinetic simulation, after which the gas leaves the discharge and cools down in the afterglow region.

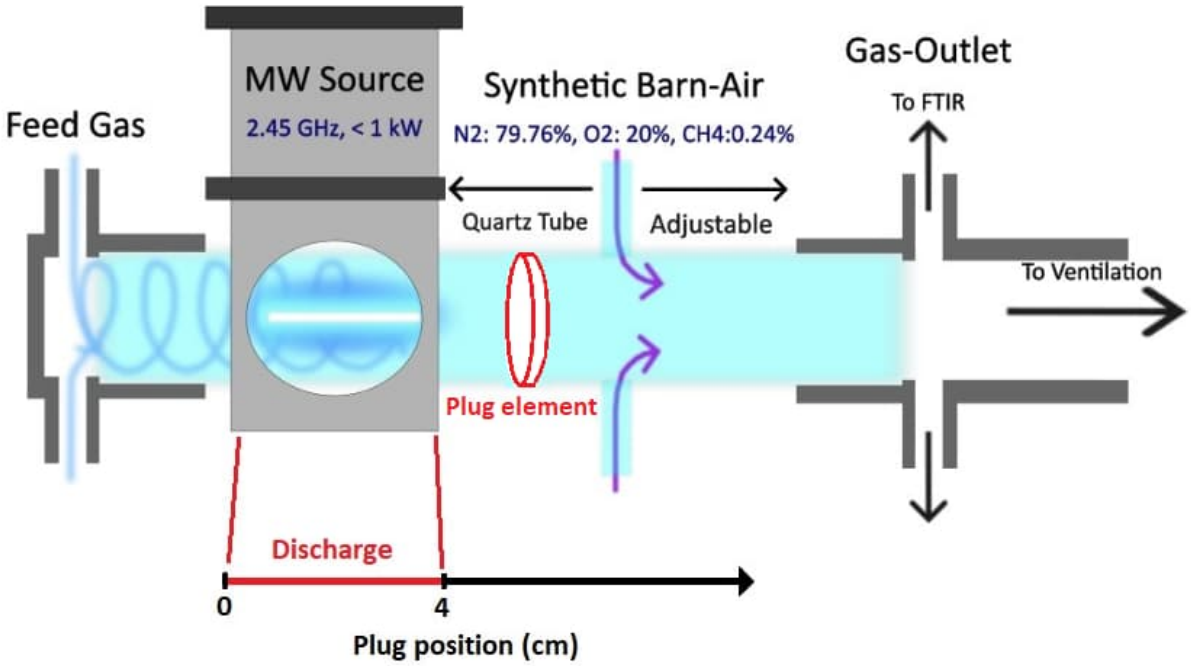

Figure 1. Schematic representation of the experimental set-up from UM and its relationship to the plug position in the kinetic simulation.

2.1.1.1 MODEL DESCRIPTION:

In order to provide a complete picture of the plasma chemistry, we consider reactions between the following neutral and charged species: $O_2(X^3\Sigma_g^-, v = 0\text{-}4)$, $O_2(a^1\Delta_g)$, $O_2(b^1\Sigma_g^+)$, $O_2(A'^3\Delta_u, A^3\Sigma_u^+, c^1\Sigma_u^-)$ (hereby referred to as O_2, O_2(a), O_2(b) and O_2(Hz)), as well as $O(^3P)$ (referred to as O), $O(^1D)$, $O(^1S)$, $O(^3P^0)$, O_3, O^+, O_2^+, O_4^+, O^-, O_2^-, O_3^-, O_4^- and electrons. In total, the model counts 58 electron impact reactions and 195 heavy particle reactions.

We solve the 0D mass-fraction balance equations for all the heavy particle densities in the plasma, according to:

$$\rho \frac{d(w_i)}{dt} = R_i \cdot M_i \qquad (1)$$

where ρ is the mass density, w_i is the mass-fraction of the species i, M_i is the molar mass and R_i is the source term resulting from electron impact reactions and volume and surface reactions. The mass density is evaluated

Funded by the European Union

at constant pressure.

The plasma chemistry is coupled to the electron Boltzmann equation solved in a two-term expansion of spherical harmonics, including electron-electron collisions. The reduced electric field, which serves as input to the Boltzmann solver, is calculated via the following expression:

$$\frac{E}{N} = \sqrt{\frac{P_d}{\sigma}} = \sqrt{\frac{P_d}{q\mu n_e}} \quad (2)$$

where P_d is the power density, σ is the conductivity, q is the electron charge, μ is the electron mobility and n_e is the electron density. The rate-balance equation for the electrons is not solved, as quasi-neutrality is imposed via $n_e = n_i - n_n$, with n_e the electron density, n_i the total positive ion density and n_n the total negative ion density.

To calculate the gas temperature self-consistently, we solve the following heat balance equation:

$$\rho C_p \frac{dT}{dt} = Q_{gas} - \frac{8\lambda_e (T - T_{nw})}{R^2} \quad (3)$$

where ρ is the mass density, C_p is the heat capacity, Q_{gas} is the total net power per unit volume transferred to gas heating, λ_e is the effective thermal conductivity of the gas mixture and R is the radius of the parabolic temperature profile (equal to the plasma radius in the contracted mode of the microwave plasma). In addition, to account for vibrational non-equilibrium, we solve the vibrational energy balance equation.

Lastly, the species densities inside the plug element can be linked to a position in the plug at each point in time, according to:

$$dx = v\, dt \quad (4)$$

where dx is the gas displacement in the plug (cf. figure 1) and v is the gas flow velocity. The acceleration of the flow due to variations in temperature and number density is given by:

$$\frac{dv}{dt} = \frac{v}{T}\frac{dT}{dt} + \frac{RT}{p} R_{tot} v \quad (5)$$

where R_{tot} is the total production/loss rate of particles due to dissociation/recombination processes.

2.1.1.2 MODEL VALIDATION:

Since we could not find experimental data for pure O_2 plasma at atmospheric pressure, we first extensively validated our model at low pressure (1-10 Torr) where very good experimental data are available. Good agreement between our model and experiments was achieved for the reduced electric field **[2]**, gas temperature **[2]** and the densities of the dominant neutral species, i.e. O_2(a) **[3]**, O_2(b) **[4]** and O **[2]**, as well as charged species, i.e. O^- and electrons **[5]**. In figure 2, we compare the calculated fraction of O atoms with VUV **[3]** and actinometry **[2]** measurements. Reasonable agreement between experimental data and model is achieved when using the corresponding recombination probability, γ, obtained from the experimental measurements. More extensive model validation is presented in our paper. **[1]**

In addition to the low-pressure validation, we compare our model predictions with the thermodynamic equilibrium composition of an oxygen mixture at atmospheric pressure, calculated in **[6]**. As shown in figure 3, our model aligns very well with the thermodynamic equilibrium densities.

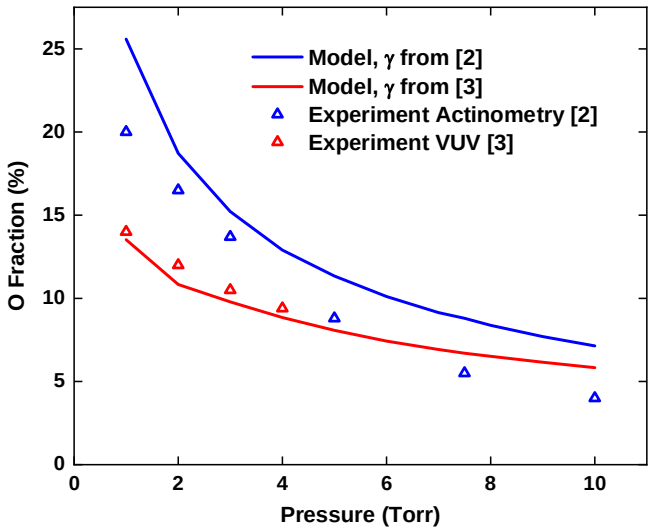

Figure 2: Comparison between model calculations and experimental results for the O fraction as a function of the gas pressure, for a discharge current of 30 mA. The blue and red line represent the O fractions obtained using the recombination probability of [2] and of [3], respectively.

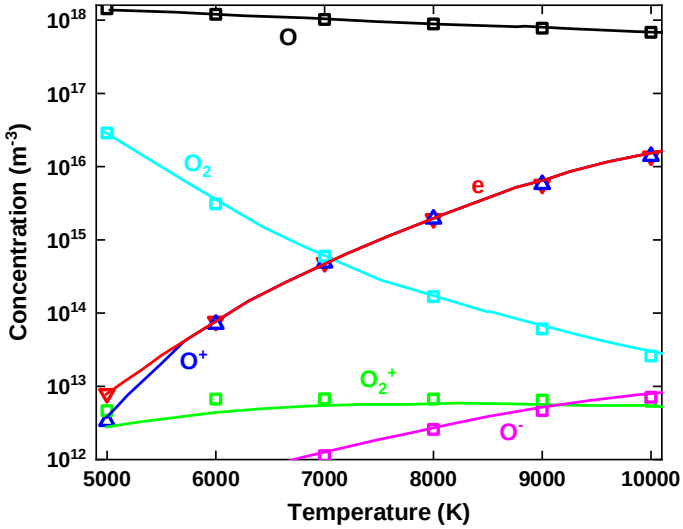

Figure 3: Comparison between model calculations and thermodynamic equilibrium calculations [6] of the dominant neutral and charged species densities as a function of the gas temperature.

2.1.1.3 MODELING RESULTS:

To explore the O atom kinetics under different plasma conditions, we ran the plug flow model for different pressures between 0.1 and 1 atm, keeping the molar flow rate and specific energy input (SEI) constant. Note that we did not consider pressures below 0.1 atm, as these low pressures are unsuitable for gas conversion applications due to costs associated with vacuum equipment. Since we are using a microwave plasma with 2.45 GHz field frequency for the CANMILK project, we applied the “effective DC field approximation” to calculate the effective electric field, used in equation (2). The power density profile, representing the plasma

discharge (cf. figure 1), increases linearly from 0 cm to its maximum value at 0.8 cm, and then linearly decreases from 3.2 cm till it reaches 0 at a distance of 4 cm.

Figure 4 shows the calculated fraction of O atoms present in the plasma and its afterglow for p = 0.1 atm and p = 1 atm, represented by the black lines, for a power of 1200 W and a molar flow rate of 20 slm, resulting in an SEI of 1656 kJ/mol, considering that only 5 % of the molar flow passes through the plasma volume. In both pressure conditions, a maximum O fraction of ca. 92 % is reached at the end of the discharge, pointing towards a very high O_2 dissociation degree. However, the drop in O atom density over the plug position in the plasma afterglow is considerably slower for p = 0.1 atm than for p = 1 atm, due to the lower rate of three-body recombination of the O atoms, and the higher flow velocity associated with a higher volumetric flow rate at lower pressure.

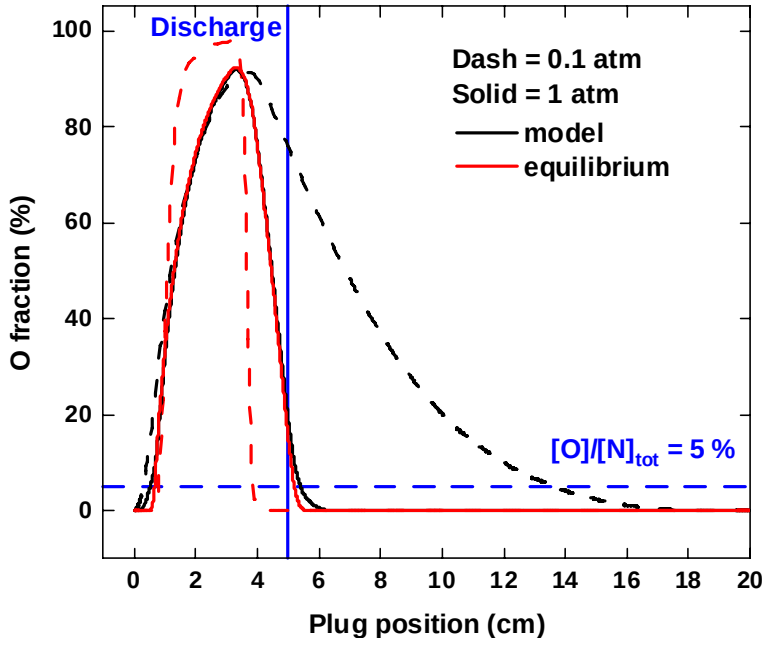

Figure 4: Calculated fraction of O atoms as a function of the position in the plug, for p = 0.1 atm (dashed) and p = 1 atm (solid), for a power of 1200 W and a flow rate of 20 slm, resulting in an SEI of 1656 kJ/mol. The red lines indicate the O fraction calculated from chemical equilibrium for the temperature specified by the model. The horizontal blue dashed line indicates an O fraction of 5 %, and the vertical blue solid line indicates the end of the discharge.

The red curves in figure 4 represent the fraction of O atoms that would be present at thermodynamic equilibrium at the calculated temperature of the model. Although the plasma reaches slightly higher temperatures at the end of the discharge for p = 1 atm (slower conductive cooling at higher pressure), figure 4 illustrates that the equilibrium O atom fraction is higher for p = 0.1 atm. This is due to the principle of Le Chatelier, which favours the formation of dissociated products at lower pressures. However, the maximum O fraction predicted by our model is roughly the same for both pressure conditions. This arises from the fact that, for p = 1 atm, the O atom fraction can reach its upper limit, i.e. the O atom fraction corresponding to thermodynamic equilibrium at the given plasma temperature, whereas for p = 0.1 atm, the dissociation rate is too slow to reach this dissociation limit.

Due to the rapid cooling of the gas upon exiting the discharge, the thermodynamic equilibrium O atom density (red dashed line) is immediately quenched after the gas leaves the discharge, while according to our kinetic model, the atoms travel a significant distance, due to the limited three-body recombination kinetics and relatively high flow velocity. In contrast to the large deviation between the equilibrium O fraction and the result

Funded by the European Union

from our kinetic model at p = 0.1 atm, figure 4 indicates that the calculated O fraction at p = 1 atm closely follows the equilibrium O fraction throughout the complete simulation. The close agreement is a result of rapid reaction kinetics at atmospheric pressure and the slower rates of gas heating and cooling, as compared to lower pressures. Consequently, it is important that the afterglow does not cool significantly below a temperature of 2400 K, as this is the temperature at which the equilibrium fraction of O atoms drops below 5 %.

To evaluate how far the O atoms travel in the plasma afterglow, we arbitrarily defined a minimum O fraction of 5% as the threshold for the O atoms to be still significantly present, indicated by the dashed blue line in figure 4. Adopting this critical density, the radicals are able to travel 9.7 cm (i.e., till 13.7 cm, since the discharge ends at 4 cm) for p = 0.1 atm after they have left the discharge, while they only reach 1.4 cm after the discharge (i.e., till 5.4 cm) for p = 1 atm.

We can define the lifetime of the O atoms as the time interval between when the gas exits the discharge and when the O atoms disappear in the plasma afterglow, i.e., where they drop below the critical O fraction of 5 %. In this way, we obtain a lifetime of 3.8 ms at p = 0.1 atm, and a lifetime of 1.8 ms at p = 1 atm. Note that although the three-body recombination frequency (1/s) of O increases by two orders of magnitude going from p = 0.1 atm to p = 1 atm at a given temperature, the O atom's lifetime at p = 0.1 atm is only approximately twice as long as that at p = 1 atm. This can be attributed to the slower cooling of the plasma afterglow at higher pressure, leading to increased O creation and diminished O recombination in the afterglow.

Since we would like to work at atmospheric pressure in the current project, these modelling results might give the impression that, due to the relatively short O atom lifetimes and travel distances in the afterglow, it is challenging to obtain mixing of the plasma afterglow with the barn air before the O atoms recombine. However, due to the 0D-framework of the model, the heat balance and resulting temperature profile in the plasma afterglow are very approximate. As shown in equation 3, all heat loss is described by conductive cooling assuming a parabolic radial temperature profile. To prevent the plasma from reaching unphysically high temperatures, we chose a very narrow temperature profile (by assuming it is equal to the plasma radius). Since we adopt the same radius of the temperature profile in the plasma afterglow, conductive cooling is likely overestimated. If a higher temperature can be sustained in the plasma afterglow, the lifetime of the O atoms will increase. A more precise understanding of the temperature profile in the plasma afterglow, through either experimental data from UM or advanced fluid modeling within PLASMANT, will enable more accurate predictions in this regard.

Although Raman measurements for gas temperature and O atom density are not yet available, FTIR measurements conducted by UM, which assessed the downstream CH_4 conversion, suggest significant CH_4 conversion still occurs when barn air is injected 14 cm after the plasma ends. This implies that the oxygen afterglow remains above 1000 K, whereas our calculations indicate that the afterglow has already cooled to room temperature at this point. This discrepancy suggests that the afterglow in the experimental setup at UM indeed cools more slowly than in our simulations, resulting in longer O atom lifetimes. Therefore, rather than focusing on the absolute values of O atom lifetime and travel distance predicted by the model, the key takeaway should be that O atoms immediately relax to their equilibrium density at atmospheric pressure when the afterglow cools down. Consequently, since the afterglow contains an equilibrium fraction of O atoms, the modeling results highlight the importance of preventing the afterglow from cooling significantly before mixing with the barn air, to avoid substantial O atom loss. Practically, this means that barn air should be injected as close to the end of the discharge as possible, and it may be advantageous to insulate the reactor walls to minimize conductive heat losses.

2.1.2 MODEL 2: O_2 AFTERGLOW/BARN AIR MIXING MODEL

The aim of the second model is to study the interaction of the plasma afterglow with the barn air mixture. More specifically, we want to study how the O atoms created in the plasma, activate the CH_4 molecules, ideally resulting in complete conversion of the CH_4 fraction.

2.1.2.1 MODEL DESCRIPTION:

The initial composition (O_2/O mixture) of the calculation represents the O_2 plasma afterglow. Since the oxygen plasma model indicated that the composition of the O_2 afterglow is at thermodynamic equilibrium at atmospheric pressure, we can easily calculate the ratio of O atoms present at the start of the simulation by means of the equilibrium constant for O_2 dissociation, evaluated at the afterglow temperature, i.e. the initial temperature of the simulation.

The mixing of the CH_4 containing atmosphere with the O_2 afterglow is simulated by adding a source term to the (N_2, O_2, CH_4) species, defined by the following mixing rate (MR):

$$MR\ [\text{mol/ s}] = a * n * v_{mix}[1/\text{s}] * \exp(-v_{mix}[1/\text{s}] * \text{t}) \quad (6)$$

where n is the number of moles in the O_2 plasma afterglow, a determines how many times n (with N_2/O_2/CH_4 composition) is added to the system, i.e. the ratio of the barn air flow rate over the plasma flow rate, and v_{mix} is the mixing frequency determining the rate of mixing.

The gas mixture is cooled down through mixing with the cold gas:

$$C_p \frac{dT}{dt} = Q_{reactions} - MR * (H(T) - H(T_0)) \quad (7)$$

where $H(T_0)$ and $H(T)$ are the enthalpy of the barn air at room temperature and at the temperature of the O_2/barn air mixture, respectively. Note that the mixing term in equation (7) is the only cooling term and we are not considering conductive heat losses, since we assume that in the timeframe of mixing conductive losses are negligible and the majority of the conversion occurs.

The volume is adjusted to balance variations in gas density and temperature, keeping a constant pressure.

We use the GRIMECH 3.0 mechanism **[7]**, which is a chemistry set fit to experimental results of combustion of CH_4 in air, optimized for 1000 K < T < 2500 K. We assume that the Arrhenius fits are valid outside the optimization range (i.e. T < 3500 K, the temperature range used in this work), since the elementary reactions are described by rate parameters reflecting the current good understanding of elementary reaction theory.

2.1.2.2 MODELING RESULTS:

The aim of the model is to scan a parameter range, for the temperature of the O_2 plasma afterglow, mixing ratio a (i.e., flow rate barn air/flow rate O_2 plasma) and mixing frequency v_{mix}, to optimize CH_4 conversion, minimize energy cost per CH_4 molecule and minimize NO_x production.

We start with stating some general observations. Firstly, since a high afterglow temperature is needed to have sufficient O atoms present (high dissociation degree requires high temperature for thermal plasma), the mixing ratio of barn air over oxygen plasma should be sufficiently high. Otherwise, the gas mixture will heat up to temperatures far above the temperature (around 1000 K) at which thermal conversion of CH_4 (400 ppm) occurs (where the CH_4 fraction reacts away spontaneously within 1 s), and the process is per definition less energy efficient than simply heating the barn air, since the energy required to heat up the oxygen gas would be just a waste of energy.

Secondly, NO_x will be formed due to the high temperature of the plasma afterglow, needed for sufficient O atoms to be present, but the production can be minimized through fast mixing (see below). Therefore, we need to look for conditions where the NO_x concentration can be kept under acceptable limits, while there is still sufficient CH_4 conversion.

Figure 5 shows the calculated CH_4 conversion for a CH_4 fraction of 400 ppm (highest CH_4 concentration measured in the barn) and a mixing ratio of a = 8 (flow rate of barn air is 8 times higher than the plasma flow rate), as function of the O_2 afterglow temperature, for three different mixing frequencies. Obviously, the CH_4 conversion increases with increasing afterglow temperature, since it corresponds with a higher O atom density in the afterglow. In general, the model predicts that CH_4 can be converted up to 100%, for afterglow temperatures around 3400 K and sufficiently high mixing frequency.

Figure 5 also indicates that the mixing rate influences the CH_4 conversion, where higher conversions can be reached at higher afterglow temperatures for higher mixing frequencies. However, at lower afterglow temperatures, the opposite is seen, where a lower conversion is reached for higher mixing frequencies. This can be attributed to two competing effects. First, faster mixing corresponds to faster cooling. As a result, for a certain number of moles of barn air added to the system, which corresponds to a specific gas mixture temperature (since cooling is only determined by the number of moles of cold gas added to the system), more O atoms will be present since they have had less time to recombine. In this way, more O atoms are in contact with CH_4 molecules, enhancing the CH_4 conversion. Secondly, O atoms react more effectively with CH_4 at higher temperatures. As a result, the rate of CH_4 activation by O atoms will strongly decrease with respect to the rate of O atom recombination at lower temperatures. In this way, fast cooling reduces CH_4 conversion. At lower afterglow temperatures, the second effect dominates and faster mixing decreases the overall conversion. At higher afterglow temperatures, the first effect is more important and a higher mixing rate improves the CH_4 conversion.

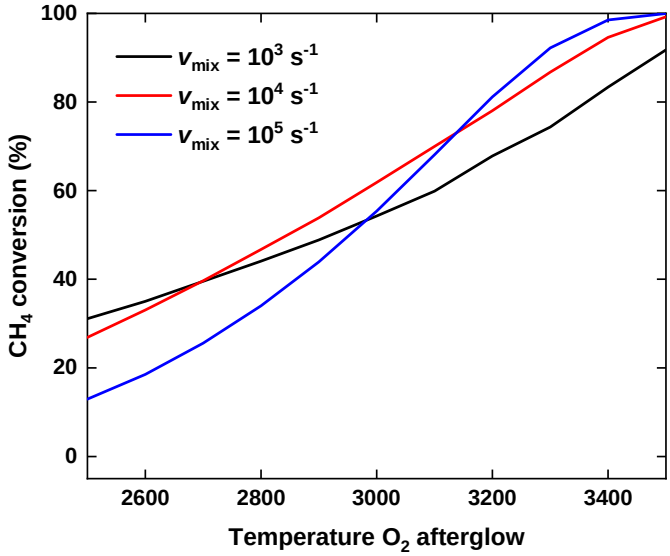

Figure 5: Conversion of CH4 (400 ppm) for a mixing ratio of a = 8, as function of the afterglow temperature, for different mixing rates.

Figure 6 depicts the calculated NO_x production for the same conditions as used above. Since the O atoms will more effectively react with N_2 at higher temperatures, the NO_x production increases with rising temperature. Figure 6 clearly illustrates that the NO_x production is strongly reduced upon increasing mixing rate, since a faster cooling rate decreases NO_x formation. However, the mixing rates used are very high already, corresponding to mixing of all the barn air with the O_2 plasma afterglow within 5 ms, 0.5 ms and 0.05 ms, for the mixing frequencies of 10^3, 10^4 and 10^5 s^{-1}, respectively. Note that at the lowest mixing rate of v_{mix}= 10^3 s^{-1}, the NO_x production is already quite high at temperatures corresponding to CH_4 conversion above 50 %, indicating that mixing frequencies below 10^3 s^{-1} would probably be unsuitable for the application. These results are pure model predictions, and will need to be experimentally validated, but the high mixing rates might require a challenging reactor set-up.

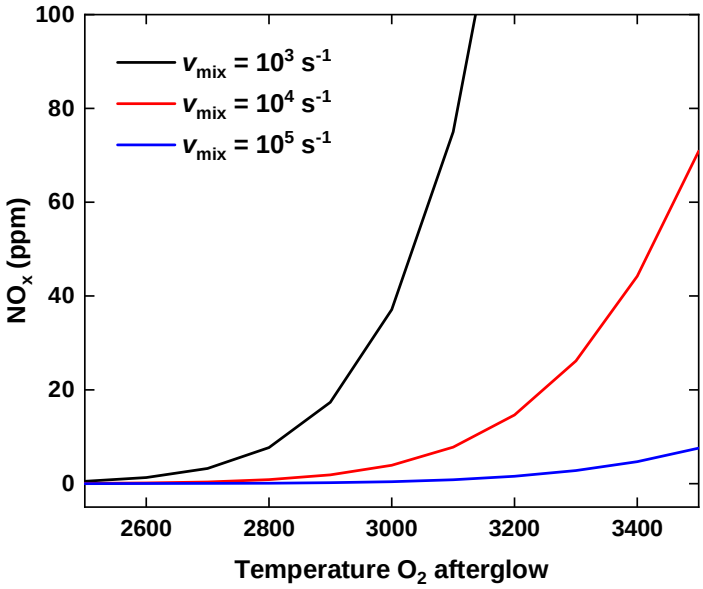

Figure 6: NOx production for a CH4 fraction of 400 ppm and a mixing ratio of a = 8, as function of the afterglow temperature, for different mixing rates.

Figure 7 presents the energy cost per moles of degraded CH_4, again for the same conditions as discussed above. The energy cost per mole of CH_4 is calculated as the energy required to heat up (and dissociate) the oxygen gas to the afterglow conditions, divided by the number of moles of converted CH_4. Note that this is the ideal limit, since energy will also be lost through wall losses in the discharge, and the plasma afterglow will cool down before it mixes with the barn air at the injection point.

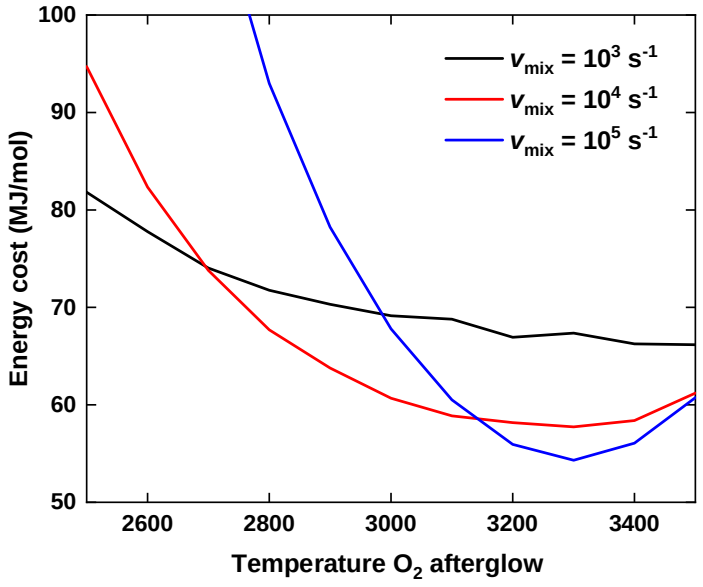

Figure 7: Energy cost per mole of degraded CH4, for a CH4 fraction of 400 ppm and a mixing ratio of a = 8, as function of the afterglow temperature, for different mixing rates.

Figure 7 illustrates how the energy cost per mole of CH_4 decreases with increasing temperature, since the

improved conversion outweighs the higher energy input. Only at high conversion (>90%), the energy cost increases with increasing temperature, because it costs more energy to convert the small fraction of remaining CH_4. For appropriate conditions (high afterglow temperature and high mixing rate), the energy cost can be reduced to values around 55 MJ/mol.

In summary, figure 5 and 7 illustrate that a high afterglow temperature (T > 3200 K) is needed to have sufficient CH_4 conversion (> 80 %) and to reach the lowest energy cost. As a result, to avoid significant NO_x formation, high mixing rates, around 10^5 s^{-1}, are needed to achieve rapid cooling of the plasma afterglow, as indicated in figure 6.

We also tested the effect of using different mixing ratios of barn air vs. O_2 plasma afterglow. Figure 8 shows the CH_4 conversion as function of the O_2 afterglow temperature for different mixing ratios, for a CH_4 fraction of 400 ppm and a mixing frequency of ν_{mix} = 10^4 s^{-1}. As the ratio of barn air/O_2 plasma increases, higher afterglow temperatures are needed to reach the same conversion, since more O atoms need to be present to convert the higher amount of CH_4 molecules, and the cooling due to the mixing with barn air will be stronger (leading to faster recombination of O atoms).

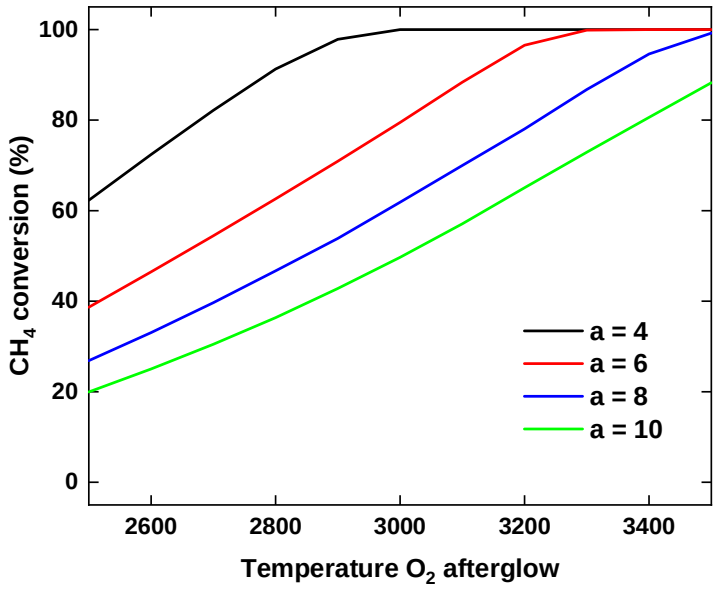

Figure 8: Conversion of CH4 (400 ppm) for a mixing frequency of ν_{mix} = 10^4 s^{-1}, as function of the afterglow temperature, for different mixing ratios (a).

Figure 9 illustrates the NO_x production as function of the O_2 afterglow temperature for the different mixing ratios, for the same conditions as used above. The formation of NO_x clearly decreases as the volume of barn air increases, attributed to the enhanced cooling rate resulting from a higher ratio of cold gas (i.e., barn air) to hot plasma afterglow. However, considering that higher temperatures are needed for higher ratios of barn air/O_2 plasma to reach the same CH_4 conversion, for a given conversion degree, the NO_x formation will increase at higher mixing ratios of barn air/O_2 plasma.

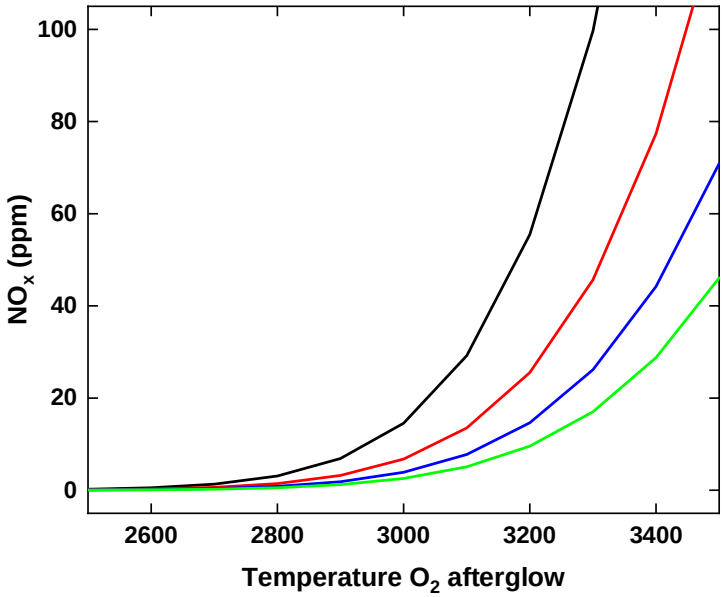

Figure 9: NOx production for a CH4 fraction of 400 ppm and a mixing frequency of ν_{mix} = 10^4 s^{-1}, as function of the afterglow temperature, for different mixing ratios.

Figure 10 presents the energy cost per mole of degraded CH_4 molecules as function of the O_2 afterglow temperature for the different mixing ratios, again for the same conditions as used above. As the amount of barn air increases compared to the plasma afterglow, the energy cost can be significantly reduced since we can convert larger amounts of CH_4. However, since this requires higher afterglow temperatures, also the NO_x production will increase.

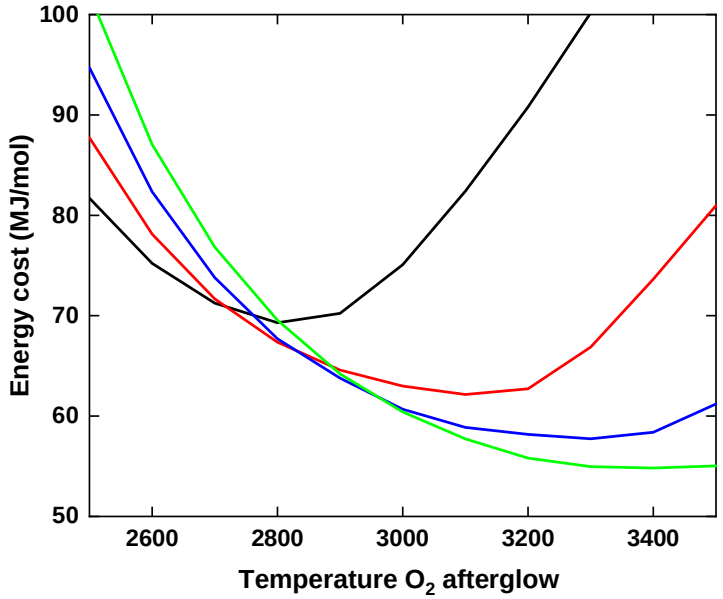

Figure 10: Energy cost per mole of degraded CH4, for a CH4 fraction of 400 ppm and a mixing frequency of ν_{mix} = 10^4 s^{-1}, as function of the afterglow temperature, for different mixing ratios.

In summary, we can achieve a lower energy cost at higher barn air/O_2 plasma ratios, but since this requires a high afterglow temperature, this will also lead to increased NO_x production. Therefore, we should aim for the

highest possible mixing ratio of barn air/O_2 plasma, where NO_x production is still acceptable.

Of course, the high mixing ratio still needs to be achievable from a practical point of view, since this would require a much higher flow rate of barn air with respect to O_2 plasma. Note, however, that the plasma afterglow simulated in this work represents the inner hot plasma region flowing out of the microwave discharge. In reality, not all the oxygen gas flowing through the microwave discharge will pass through the plasma, and thus, heat up to the afterglow temperature representing the inner hot plasma region. Consequently, the actual ratio of barn air flow rate to the flow rate of the oxygen plasma could be lower than the values discussed above. This consideration eases the constraints on the experimental conditions.

Utilizing an effective CH_4 adsorber, as is also being considered within the CANMILK project, opens the possibility for higher CH_4 fractions to be treated. By concentrating the CH_4 fraction, the energy cost per mole of CH_4 can be significantly reduced, since the O atoms will more effectively react with CH_4. Figure 11 compares the CH_4 conversion as function of the O_2 afterglow temperature, for a CH_4 fraction of 400 and 2400 ppm. It is clear that for temperatures above 3300 K where we have sufficient CH_4 conversion, only a slight temperature increase (< 100 K) is needed for a CH_4 fraction of 2400 ppm to achieve the same conversion (i.e., near 100%) as for a CH_4 fraction of 400 ppm, while 6 times the amount of CH_4 is converted. As a result, the energy cost per moles of CH_4 will be approximately 6 times lower.

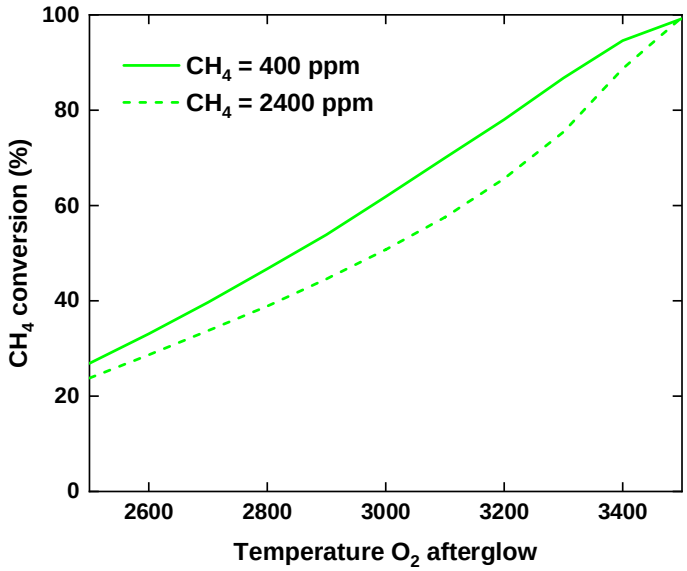

Figure 11: CH4 conversion for a CH4 fraction of 400 ppm and 2400 ppm, for a mixing ratio of a = 8 and a mixing frequency of ν_{mix} = 10^4 s^{-1}, as function of the afterglow temperature.

In conclusion, our modeling calculations suggest that O atoms in the O_2 plasma afterglow can effectively remove the low concentrations of CH_4 present in barn air, provided that the afterglow temperature remains sufficiently high. Besides the high afterglow temperature, a high mixing ratio and mixing rate are required to reduce the energy cost and minimize NO_x formation.

On the other hand, next to the O atom-driven post-plasma conversion of CH_4, we are also exploring an alternative strategy involving the production of NO_x species in an air plasma, which are then used to oxidize CH_4 at the catalyst surface. This approach offers several advantages: it allows the use of regular barn air as the plasma feed gas instead of more expensive pure oxygen. In addition, NO_x species have a significantly longer lifetime compared to O atoms and can exist at lower temperatures, making them more effective for oxidizing CH_4 at the moderate temperatures found at the catalyst surface. Importantly, within this strategy, NO_x would be produced in a controlled manner, ensuring its concentration matches the CH_4 concentration in the

barn air. This way, all the NO_x would react with CH_4 at the catalyst surface, preventing any NO_x emissions into the atmosphere. We believe this is a very promising alternative strategy to be explored for this project.

2.2 T2.2: COMPUTATIONAL FLUID DYNAMICS MODEL

In addition to the above chemical kinetics models, predicting the post-plasma conversion, we also developed a CFD model, in order to evaluate the mixing of the O_2 plasma afterglow with the barn air mixture. As indicated by the previous chemical kinetics modeling results, rapid mixing is crucial for efficient CH_4 conversion and reduced NO_x formation. Therefore, the developed CFD model can be utilized to optimize the reactor geometry for enhanced mixing of the plasma afterglow and barn air.

2.2.1 MODEL DESCRIPTION:

The gas flow is modeled using the compressible Navier-Stokes fluid equations. Since we consider steady-state solutions, we can neglect terms containing the time derivative in the equations.

$$\nabla(\rho * \boldsymbol{u}) = 0 \tag{8}$$

$$\rho(\boldsymbol{u} * \nabla)\boldsymbol{u} = -\nabla p + (\mu + \mu_T)\nabla^2\boldsymbol{u} \tag{9}$$

Here, ρ is the gas density, $\boldsymbol{u}$ is the flow velocity, p is the pressure and μ and μ_T are the dynamic and turbulent viscosity, respectively. The latter is calculated by the SST turbulence model.

The heat transfer is modelled using the heat balance equation, which is coupled to the Navier-Stokes equations:

$$\rho C_p \boldsymbol{u} * \nabla T = -\nabla * (-k\nabla T) \tag{10}$$

where C_p is the heat capacity. Note that we do not consider a heat source, given that the elevated temperature of the plasma afterglow is defined by a high inlet temperature.

Lastly, the transport of species is described according to the following equation:

$$\rho(u \cdot \nabla)\omega_i = \nabla\left(\rho D_i^m \nabla\omega_i + \rho\omega_i D_i^m \frac{\nabla M_n}{M_n} - \boldsymbol{j}_{c,i}\right) \tag{11}$$

where ω_i is the mass fraction of species i and M_n is the mean molar mass. The diffusive flux is approximated by Fick's law with the effective mixture-averaged diffusion coefficient D_i^m. The last term on the right hand side corresponds to a corrective flux that enforces a zero net diffusive flux. Note that equation (11) does not contain a source term resulting from chemical reactions, since we do not solve the chemistry in the current CFD model. However, the aim is to couple the chemistry (as described in T2.1) to the flow in a future stage.

2.2.2 MODELING RESULTS:

To evaluate the mixing efficiency in the reactor, we need to define an analytical expression that takes as input some output variables of the CFD simulation, i.e. species molar concentrations, and yields a measure of the mixing degree in the point of interest. Therefore, we defined the following expression for this mixing degree, as a function of radial position, M(r):

$$M(r) = \begin{cases} R/R_i\,, & for\ R < R_i \\ R_i/R\,, & for\ R > R_i \end{cases}, \qquad R = c_{CH_4}/c_{O_2}\,,\ R_i = F_{CH_4,i}/F_{O_{2,i}} \tag{12}$$

where c_{CH_4} and c_{O_2} are the molar concentrations of CH_4 and O_2, and $F_{CH_4,i}$ and $F_{O_{2,i}}$ are their inlet molar flow rates. This expression provides a value where 1 denotes perfect mixing, and 0 means no mixing (either only CH_4 or only O_2 present).

To assess whether the current experimental set-up in Maastricht University achieves rapid mixing, we modelled their reactor geometry, shown in figure 12. Oxygen gas flows through a 2.6 cm diameter quartz tube, and the microwave plasma is created where the tube passes through the microwave cavity. Following the discharge, two tangential inlets with a 4 mm diameter are positioned at an adjustable distance to introduce barn air into the O_2 afterglow. The plasma afterglow is simulated by considering an O_2 inlet flow at 1000 K. For simplicity, the barn air is simulated here in first instance as pure CH_4, entering in the tangential inlets at a temperature of 300 K.

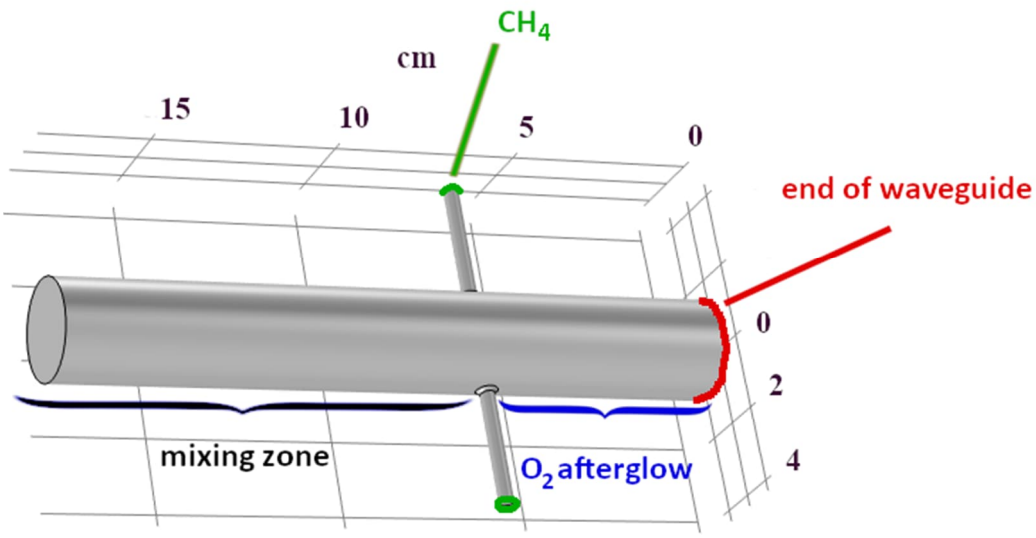

Figure 12: Reactor geometry of the experimental setup at Maastricht University

Figure 13 illustrates the mixing of a 5 slm O_2 flow with a 5 slm CH_4 flow, by plotting the mixing degree (given by equation 12) on cut planes of the reactor. Because the cut plane at the end of the simulated domain is not completely red, we can conclude that complete mixing is not yet achieved. Since this corresponds to a distance of 12 cm after the injection point of CH_4, over which the plasma afterglow likely cools down substantially, thus losing a significant amount of O atoms, the mixing rate resulting from a 5 slm O_2 and CH_4 flow appears too low for the application.

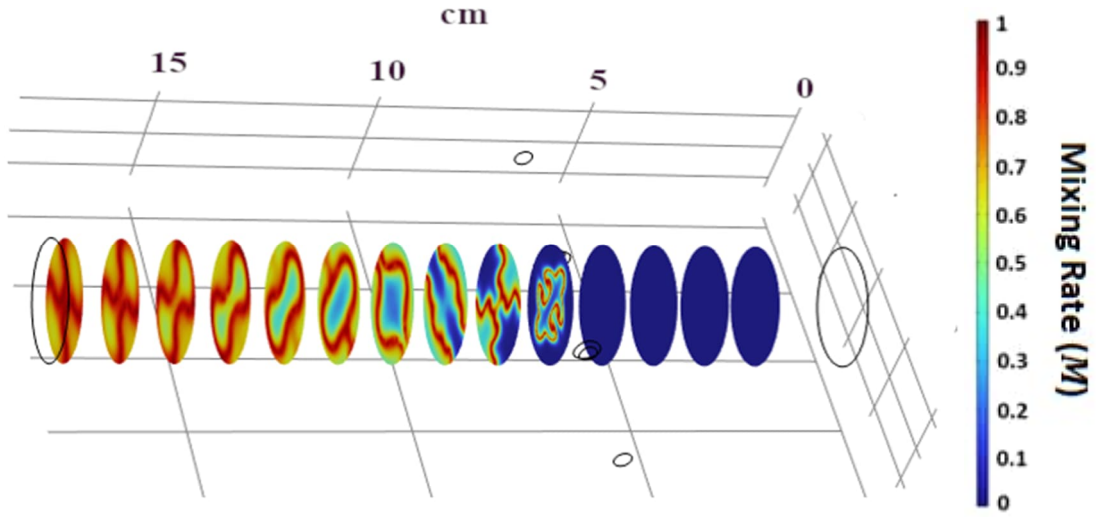

Figure 13: Mixing degree of O_2 and CH_4, for an O_2 and CH_4 flow rate of 5 slm.

Figure 14 shows the mixing for a 5 slm O_2 flow with a 10 slm CH_4 flow. Clearly, increasing the tangential flow of CH_4 strongly improves the mixing rate, potentially due to better penetration of the O_2 flow by the CH_4 flow. Since a high ratio of barn air flow over O_2 flow is desirable for a favorable energy efficiency, as predicted from our chemical kinetics model (T2.1), the current setup may be suitable for inducing fast mixing at high barn air flow rates. In future work, conditions (vortex flow, flow rate and temperature) closer to the experimental conditions at Maastricht University can be modeled to evaluate the mixing performance in their experiments.

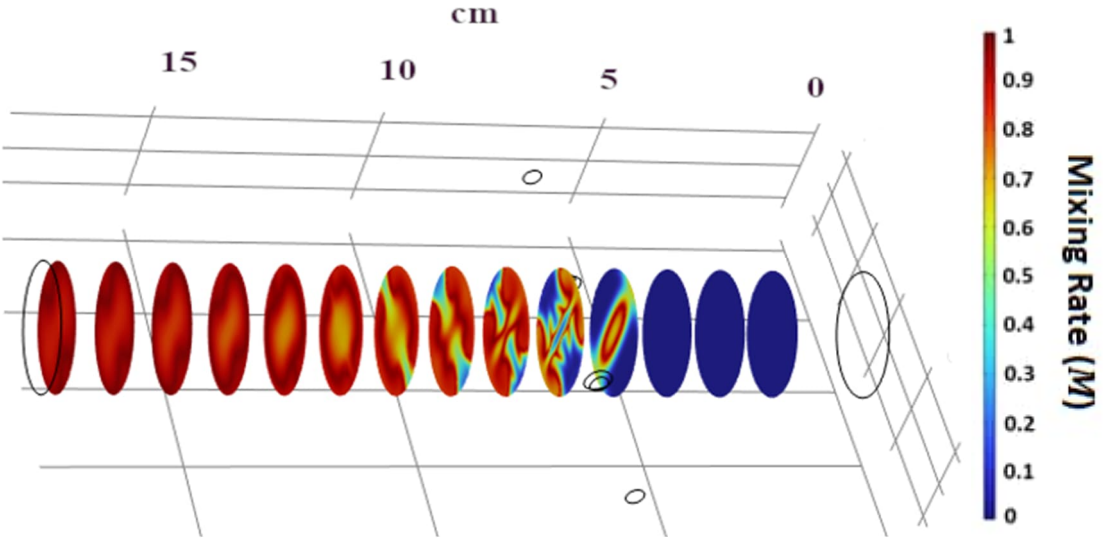

Figure 14: Mixing degree of O_2 and CH_4, for an O_2 flow rate of 5 slm and CH_4 flow rate of 10 slm.

3 CONCLUSIONS

We have developed two distinct chemical kinetics models. In the first model, we describe the oxygen plasma chemistry with the aim of investigating the O atom densities in the O_2 plasma afterglow. Model calculations indicate that, at atmospheric pressure, the O atoms instantly relax towards their equilibrium densities, given by the dissociation equilibrium at the afterglow temperature, as the afterglow cools down. As a result, the O_2 afterglow should be kept at sufficiently high temperatures (> 2500 K) to have a substantial radical fraction present. Given our intention to operate at atmospheric pressure, injecting barn air should ideally occur as close to the end of the discharge as possible to prevent a significant amount of O atoms from recombining before the afterglow mixes with the barn air.

At lower pressures (0.1 bar), O atom three-body recombination is notably slower, resulting in a more gradual relaxation of the O atom density toward its equilibrium value. However, since conductive cooling is more effective at lower pressures, the afterglow cools more rapidly, enhancing radical recombination and resulting in comparable O atom lifetimes for p = 0.1 bar (i.e. 3.8 ms) and p = 1 bar (i.e. 1.8 ms).

The composition of the oxygen plasma afterglow, obtained from the first model, acts as input to the second model, in which we evaluate how efficiently the O atoms convert the low CH_4 fraction. The modelling results indicate that the majority of the O atoms present in the afterglow will recombine to O_2 upon cooling of the hot afterglow through mixing with the cold barn air. Consequently, a high initial O atom fraction in the O_2 afterglow, necessitating high afterglow temperatures (> 3000 K), is required to convert the small fraction of CH_4 (e.g., 400 ppm). These high afterglow temperatures also mean that a significant amount of NO_x will be formed, but the results show that the NO_x formation can be minimized through fast mixing of the O_2 afterglow with the barn air.

Therefore, a high afterglow temperature, mixing ratio and mixing rate are desirable for optimizing energy efficiency and minimizing NO_x production, e.g., an afterglow temperature of 3300 K with a = 8 and v_{mix} = 10^4 s^{-1} yields a CH_4 conversion of 87 % with an energy cost of 58 MJ/mol and NO_x production of 26 ppm. These model predictions are useful to guide the experiments planned in the real (barn) setting by VTT. Of course, the model predictions first need to be validated by experiments from UM, also to evaluate whether the optimum conditions are feasible to be realized in practice.

In addition to the two chemical kinetics models, we also developed a CFD model to evaluate the mixing performance of the O_2 plasma afterglow with the barn air mixture in the current experimental set-up used at UM. The CFD results indicate that proper mixing can be achieved when the flow rate of the barn air, entering at the tangential inlets, is sufficiently high with respect to the O_2 flow rate (e.g. 5 slm O_2, 10 slm CH_4). In future work, conditions (vortex flow, flow rate and temperature) closer to the experimental conditions at UM can be modeled to provide a more precise evaluation of the mixing performance in their experiments.

Finally, next to O atom-driven CH_4 conversion, we are exploring using NO_x species produced in an air plasma to oxidize CH_4 at the catalyst surface. This alternative strategy is very promising, as it allows the use of regular barn air instead of expensive pure oxygen, and NO_x species, with their longer lifetime and stability at lower temperatures, are more effective for CH_4 oxidation at the moderate temperatures found at the catalyst surface. We will further explore this promising alternative strategy within our project.

4 BIBLIOGRAPHY

1. Albrechts, M.; Tsonev, I.; Bogaerts, A., Investigation of O atom kinetics in O2 plasma and its afterglow. Plasma Sources Science and Technology 2024, 33 (4), 045017.
2. Booth, J.-P.; Guaitella, O.; Chatterjee, A.; Drag, C.; Guerra, V.; Lopaev, D.; Zyryanov, S.; Rakhimova, T.; Voloshin, D.; Mankelevich, Y., Oxygen (3P) atom recombination on a Pyrex surface in an O2 plasma. *Plasma Sources Science and Technology* 2019, *28* (5), 055005.
3. Booth, J.-P.; Chatterjee, A.; Guaitella, O.; Sousa, J. S.; Lopaev, D.; Zyryanov, S.; Rakhimova, T.; Voloshin, D.; Mankelevich, Y.; de Oliveira, N., Determination of absolute O (3P) and O2 (a1 Δ g) densities and kinetics in fully modulated O2 dc glow discharges from the O2 (X3 Σ g−) afterglow recovery dynamics. *Plasma Sources Science and Technology* 2020, *29* (11), 115009.
4. Booth, J.-P.; Chatterjee, A.; Guaitella, O.; Lopaev, D.; Zyryanov, S.; Volynets, A.; Rakhimova, T.; Voloshin, D.; Chukalovsky, A.; Mankelevich, Y., Quenching of O2 (b1Σg+) by O (3P) atoms. Effect of gas temperature. *Plasma Sources Science and Technology* 2022, *31* (6), 065012.
5. Baeva, M.; Luo, X.; Pfelzer, B.; Repsilber, T.; Uhlenbusch, J., Experimental investigation and modelling of a low-pressure pulsed microwave discharge in oxygen. *Plasma Sources Science and Technology* 2000, *9* (2), 128.
6. Hoffmann, H., O--ion radiation in the spectrum of an oxygen arc plasma. *Journal of Quantitative Spectroscopy and Radiative Transfer* 1979, *21* (2), 163-180.
7. Gregory P. Smith, D. M. G., Michael Frenklach, Nigel W. Moriarty, Boris Eiteneer, Mikhail Goldenberg, C. Thomas Bowman, Ronald K. Hanson, Soonho Song, William C. Gardiner, Jr., Vitali V. Lissianski, and Zhiwei Qin http://www.me.berkeley.edu/gri_mech/.